



A practical FeP nanoarrays electrocatalyst for efficient catalytic reduction of nitrite ions in wastewater to ammonia

Jiangfeng Yuan^a, Hanqing Yin^b, Xiaoxin Jin^a, Dan Zhao^a, Yuan Liu^a, Aijun Du^b,
Xiaoqiang Liu^{a,*}, Anthony P. O'Mullane^{b,*}

^a Henan Joint International Research Laboratory of Environmental Pollution Control Materials, College of Chemistry and Chemical Engineering, Henan University, Kaifeng, Henan Province 475004, PR China

^b School of Chemistry and Physics, Queensland University of Technology (QUT), Brisbane, QLD 4001, Australia

ARTICLE INFO

Keywords:

Electrocatalysis
Nitrite reduction
Ammonia production
Iron phosphide
Theoretical calculations

ABSTRACT

Ammonia production is an energy-intensive process while nitrite ions are a substantial environmental pollutant, therefore the conversion of nitrite ions (NO_2^-) into ammonia (NH_3) via an electrochemical process is of great significance. Using a hydrothermal method plus a low temperature phosphating process, iron phosphide nanoarrays (FeP NA) were prepared on a Ti plate to form FeP NA/Ti, which was then used to efficiently convert NO_2^- ions into NH_3 . In a single-chamber cell using a neutral pH electrolyte, the Faradaic efficiency for nitrite to ammonia conversion reached $82.5 \pm 2.3\%$. Various parameters were optimized to ensure the high performance of FeP NA/Ti which were explained with mechanistic studies. It was found that atomic hydrogen (H^*) greatly impacts both the reaction rate and selectivity. Furthermore, density functional theory (DFT) calculations reveal that the (211) and (011) facets of FeP are the main active faces for nitrite reduction where the nitrite ions tend to bind with two adjacent Fe atoms of FeP to ensure maximum performance.

1. Introduction

Nitrite ions (NO_2^-) are classified as a category A carcinogen, where the intake of a large amount of NO_2^- by organisms may cause cancer, malformations, blue baby syndrome, brain damage and other diseases [1,2]. Therefore, many countries have strict limits on the content of NO_2^- in water. For example, the Environmental Protection Agency of the United States and World Health Organization stipulate that the NO_2^- - N content in drinking water should be less than 1 and 3 ppm, respectively. However, due to the ubiquitous use of chemical fertilizers and the lack of effective treatment methods for nitrogen pollutants in industrial and domestic wastewater, NO_2^- has become one of the most common pollutants in natural water bodies [3,4]. Consequently, the conversion of NO_2^- into harmless substances or even useful products has attracted tremendous research interest in recent years. For example, hydrogenation of NO_2^- on some noble metals (Pd, Rh, Ir) or their alloys in a concentrated H_2 atmosphere demonstrated the selective reduction of NO_2^- to N_2 or ammonia (NH_3) [5–8]. Nevertheless, the low treatment efficiency, use of inflammable and explosive H_2 , high cost and easy poisoning of precious metals limited the application of this technology

in large-scale wastewater treatment. Therefore, it is essential to develop a safe, cheap, and convenient way to treat polluted water while also contemplating the resourceful utilization of NO_2^- .

As another conversion product of NO_2^- , NH_3 exhibits a much more economical and social benefit than N_2 because it has almost doubled the world's grain output and plays a pivotal role in many industrial fields such as explosives, pharmaceuticals, food additives, printing and dyeing etc. [9–11]. In addition, NH_3 is considered as a potential carbon-free energy carrier due to its high energy density, easy storage and convenient transportation [12–15]. A significant drawback, however, is that industrial NH_3 synthesis (Haber-Bosch process) requires both high temperature ($\sim 500^\circ\text{C}$) and high pressure (~ 200 bar) to transform N_2 to NH_3 with a low conversion rate due to the large $\text{N} \equiv \text{N}$ bond energy (945 kJ mol^{-1}) [16]. As a result, this process consumes $\sim 1\%$ of the total global energy and leads to a large amount of carbon dioxide emissions [9]. Therefore, developing new technologies for the green synthesis of ammonia is of great significance to human society [17–19]. During the past years, electrocatalytic/photocatalytic techniques have been employed for the reduction of N_2 to NH_3 [20,21]. However, the extremely low NH_3 yields, the uncertainty of the nitrogen source and the

* Corresponding authors.

E-mail addresses: liuxq@henu.edu.cn (X. Liu), anthony.omullane@qut.edu.au (A.P. O'Mullane).

<https://doi.org/10.1016/j.apcatb.2022.122353>

Received 11 July 2022; Received in revised form 28 December 2022; Accepted 30 December 2022

Available online 31 December 2022

0926-3373/© 2023 Elsevier B.V. All rights reserved.

difficulty in the determination of trace ammonia has prevented the practical application of this conversion process [22–25].

In contrast to N_2 , NO_2 shows higher water solubility and a much stronger thermodynamic tendency to be converted to NH_3 , making the selective reduction of NO_2 a promising strategy to produce ammonia [16,26]. Moreover, water treatment processes produce a large amount of toxic concentrated NO_3^-/NO_2^- wastewater, which is difficult to handle [27–29]. To solve this problem, the conversion of NO_2 to valuable NH_3 can not only eliminate water pollution, but also realize the green synthesis of NH_3 , which can be easily separated from the water system [30–32].

In recent years, electrochemistry has been adopted for the reduction of NO_2 to NH_3 with high activity and selectivity. By employing electrons as the reductant, this technique avoids the use of H_2 , which reduces the operating cost, and improves the reaction efficiency and safety. For example, a full NO_2 reduction cycle was realized on a dinuclear ruthenium complex to generate NH_3 via an unusual bent type nitrido-bridged complex [33]. Although this catalyst showed high NH_3 selectivity and activity for the six-electron NO_2 reduction reaction, the scarcity/high cost of the Ru noble metal is still problematic. Accordingly, a few transition metal macrocyclic complexes were developed as homogeneous electrocatalysts to convert nitrite to ammonia, including an iron complex, and cobalt macrocyclic complexes etc. [34,35]. Nevertheless, considering the preparation and separation difficulties of the above homogeneous electrocatalysts, heterogeneous electrocatalysts may be a better option for efficient and selective nitrite reduction. For example, a Cu_3P nanowire array grown *in situ* on copper foam (Cu_3P NA/CF) and Ni nanosheet arrays with Ni vacancies ($Ni-NSA-V_{Ni}$) were found to have good catalytic activity towards nitrite reduction to ammonia [36,37]. This has attracted the attention of many researchers and led to more in-depth research. Ni_2P and TiO_{2-x} were subsequently found to also have good catalytic activity towards nitrite conversion to ammonia [38, 39].

The catalytic reduction of NO_2 to NH_3 can be described as the deoxygenation and hydrogenation of NO_2 . Previous studies have indicated that high atomic hydrogen (H^*) coverage on the catalyst is more likely to produce NH_3 during the reduction of NO_2 , however excessive H^* may cause the hydrogen evolution reaction (HER) to interfere. Therefore, an efficient catalyst should have a moderate H^* adsorption capacity to achieve the selective reduction of NO_2 to NH_3 [40,41]. As a transition metal phosphide, iron phosphide (FeP) possesses many advantages such as excellent electrical conductivity, abundance, easy preparation, low biological toxicity, and moderate H^* adsorption capability [42]. However, the catalytic reduction of NO_2 on FeP has not been studied in detail to date.

Herein, through adjusting the solvent environment of a Ti substrate in the hydrothermal process, we firstly prepared ultrathin FeOOH nanowire arrays (FeOOH NA|Ti), which were then converted to FeP nanoarrays (FeP NA|Ti) by a low temperature phosphating process. During the electrocatalytic process, FeP NA|Ti continually produced H^* during the reduction of NO_2 with a high FE, thereby avoiding the use of large amounts of dangerous H_2 gas, and thus cutting off a potential hazard of H_2 accumulation. After the morphology and composition characterization of FeP NA|Ti, the effect of applied potential and NO_2 -N concentration on NO_2 removal percentage, NH_3 selectivity and FE were investigated in detail. To explore the reaction mechanism of nitrite reduction, density functional theory (DFT) calculations were used to calculate the adsorption energy of NO_2 and the transition state energy of NO_2 reduction at different crystal facets of FeP. This work reveals that FeP NA|Ti is a promising electrocatalyst that could potentially be used in industrial and environmental fields to eliminate and recycle nitrite pollutants in water bodies.

2. Experimental section

2.1. Materials

Ti plates (99.95 %) were purchased from Qinghe County Haoxuan Metal Material Co, Ltd (China). Hydrofluoric acid (HF , $\geq 40\%$), acetonitrile (CH_3CN), Hydrazine hydrate (N_2H_4) and potassium nitrate (KNO_3) were purchased from Tianjin Kermel Chemical Reagent Co, Ltd (China). Ethanol (C_2H_6O , 99 wt %) and tert-Butanol (TBA) was ordered from Tianjin Fuyu Fine Chemical Co, Ltd (China). Nitric acid (HNO_3 , 66 wt %), hydrochloric acid (HCl , 37 wt %) were acquired from Luoyang Haohua Chemical Reagent Co, Ltd (China). Iron chloride hexahydrate ($FeCl_3 \cdot 6H_2O$), sodium hypophosphite monohydrate ($NaH_2PO_2 \cdot H_2O$), sodium nitrite ($NaNO_2$), sodium sulfate (Na_2SO_4), sulfanilamide ($C_6H_8N_2O_2S$), N-(1-naphthyl) ethylenediamine dihydrochloride ($C_{12}H_{14}N_2 \cdot 2HCl$), phosphoric acid ($H_3PO_4 \geq 85\%$), sodium hydroxide ($NaOH$), ammonium chloride (NH_4Cl), potassium sodium tartrate tetrahydrate ($C_4H_4O_6KNa \cdot 4H_2O$), p-dimethylaminobenzaldehyde ($C_9H_{11}NO$), sodium nitrite- ^{15}N ($Na^{15}NO_2$, ^{15}N 99 at %), ammonium sulfate- ^{15}N ($(^{15}NH_4)_2SO_4$, ^{15}N 99 at %), maleic acid ($C_4H_4O_4$), deuterium oxide (D_2O) and potassium iodide (KI) were purchased from Shanghai Aladdin Biochemical Technology Co, Ltd (China). Mercury iodide (HgI_2) was bought from Shanghai Rhawn Chemical Technology Co. Ltd. The ultrapure water used throughout all experiments was purified through a Millipore system. All reagents were analytical reagent grade and used without further purification.

2.2. Synthesis catalyst

2.2.1. Preparation of FeOOH NA|Ti

A Ti plate with a size of $3.5\text{ cm} \times 3.5\text{ cm}$ was immersed in a mixed acid ($V_{(HF)}: V_{(HNO_3)}: V_{(H_2O)} = 2: 8: 10$) to remove the oxide layer on the surface, then the Ti plate was taken out, washed with water and ethanol before it was dried in air.

The preparation method of FeP NA|Ti is improved on the basis of Jiang et al. [42]. Next, 2.165 g of $FeCl_3 \cdot 6H_2O$ and 6.8 g of KNO_3 were dissolved in a mixed solution containing 240 μL HCl , 24 mL water, and 56 mL acetonitrile, which was then transferred to a Teflon-lined stainless autoclave (100 mL). The pretreated Ti plate was immersed into the solution before the autoclave was kept in an electric oven at 100°C for 4 h. After the autoclave was cooled, the Ti plate was taken out, washed with water and absolute ethanol, and dried to obtain FeOOH NA|Ti.

2.2.2. Preparation of FeP NA|Ti

To synthesize FeP NA|Ti, a porcelain boat loaded with 1.0 g of $NaH_2PO_2 \cdot H_2O$ was placed upstream in a tube furnace, and the prepared FeOOH NA|Ti was placed downstream at $\sim 10\text{ cm}$ from the $NaH_2PO_2 \cdot H_2O$ source. Then, at a flow rate of $\sim 25\text{ mL } N_2 \text{ per min}^{-1}$, the tube furnace was heated to 300°C for 120 min at a heating rate of 2°C min^{-1} , and then cooled to room temperature to obtain FeP NA|Ti. The FeP loading on the Ti sheet was $\sim 3.0\text{ mg}$, which was obtained by weighing with a high-precision analytical balance.

Fe_2O_3 |Ti was obtained by calcining FeOOH NA|Ti at 500°C for 3 h in a muffle furnace. The photographs of Ti, FeOOH NA|Ti, Fe_2O_3 |Ti and FeP NA|Ti are provided in Fig.S1.

2.3. Characterization

The X-ray diffraction (XRD) pattern was obtained at a Bruker D8 Advance diffractometer (Bruker, Germany) equipped with $Cu\ K\alpha$ radiation. Energy dispersive spectrum (EDS) and scanning electron microscopic (SEM) images were obtained by a Carl Zeiss Gemini SEM 500 scanning electron microscope (Zeiss, Germany) equipped with an energy disperse spectrometer manufactured by Oxford Instrument Corporation. High-resolution transmission electron microscopic (HRTEM) images were acquired at a FEI Tecnai G20 s-twin 200 kV transmission electron

microscope (FEI, America). X-ray photoelectron spectroscopy (XPS) data were obtained at a XPS spectrometer (Thermo scientific K-Alpha), equipped with an Al K Alpha radiation source with a test energy of 1486.8 eV and a beam spot of 400 μm . The absorbance data of samples were measured with a UH-4150 UV-vis spectrophotometer (Hitachi, Japan). The *in situ* attenuated total reflection Fourier transform infrared (*in situ* ATR-FTIR) spectrum was obtained using an infrared spectrometer (Thermo scientific Nicolet IS50) equipped with a liquid nitrogen cooled MCT detector. NMR test was conducted with Bruker ascend 500.

2.4. Electrochemical measurements

A CHI 730E electrochemical workstation was used to study the electrochemical performance of NO_2^- reduction in a 50 mL single-chamber three-electrode electrolytic cell. FeP NA|Ti was employed as the working electrode with an immersion area of 9 cm^2 , while an Ag|AgCl (filled with saturated KCl solution) reference electrode, and a Pt counter electrode were used. The distance between the working electrode and counter electrode is 2 cm, and the reaction was conducted under magnetic stirring at $\sim 400\text{ rpm}$. The electrocatalytic reduction performance of FeP NA|Ti was evaluated in simulated wastewater (0.05 M Na_2SO_4 solutions containing different concentrations of $\text{NaNO}_2\text{-N}$ (40, 80, 120, 160 and 200 mg L^{-1}). Unless otherwise specified, all electrocatalytic reduction tests were performed for 90 min, the experimental temperature was room temperature, and the pH of solution was 7.10 ± 0.06 . The pH of electrolyte solution was adjusted with H_2SO_4 (1 M) or NaOH (1 M). Herein, the current densities were acquired by normalizing the measured current values to the geometric area and electrochemistry active surface area (ECSA) of the various working electrodes. In addition, the potentials relative to RHE were converted by the following formula: $E_{\text{RHE}} = E_{\text{Ag/AgCl}} + 0.198 + 0.059 \times \text{pH}$.

2.5. Determination method

2.5.1. Determination of $\text{NO}_2\text{-N}$

Griess reagent was used as the color developing agent for the determination of $\text{NO}_2\text{-N}$ [37]. The absorbance of the purple complex of $\text{NO}_2\text{-Griess}$ reagent at 540 nm is proportional to $\text{NO}_2\text{-N}$ concentration. The preparation of the Griess reagent is described as follows: 5 mL of concentrated phosphoric acid was diluted with 25 mL of water. Then 2.0 g of p-aminobenzene sulfonamide and 0.1 g of N-(1-naphthyl)-ethylenediamine dihydrochloride were successively added to the diluted phosphoric acid solution, and stirred to obtain a homogeneous solution. To determine the concentration of $\text{NO}_2\text{-N}$, 0.1 mL of Griess reagent was added to 5 mL of diluted test solution and fully mixed. After 30 min, the absorbance of the test solution at 540 nm was measured by a UV-vis spectrophotometer. The corresponding standard curves and calibration curve are shown in Fig.S2.

2.5.2. Determination of $\text{N}_2\text{H}_4\text{-N}$

The concentration of N_2H_4 was measured using the Watt and Christp method [43]. The absorbance of N_2H_4 mixed with color reagent at 460 nm has a linear relationship with N_2H_4 concentration. The color reagent is composed of 2 g of $\text{C}_9\text{H}_{11}\text{NO}$, 10 mL of concentrated HCl and 100 mL of $\text{C}_2\text{H}_5\text{OH}$. To determine the concentration of N_2H_4 in electrolyte solution, 4 mL of electrolyte solution was mixed with 4 mL of color reagent and shaken for 15 min, then its absorbance at 460 nm was measured by a UV-Vis spectrophotometer. The UV-vis spectra and corresponding calibration curve are shown in Fig.S3.

2.5.3. Determination of $\text{NH}_3\text{-N}$

Nessler's reagent was used as the color developing agent for the detection of $\text{NH}_3\text{-N}$ [37]. The $\text{NH}_3\text{-Nessler's}$ reagent complex shows a color of brown-yellow, and its absorbance at 420 nm shows a good linear relationship with the concentration of the complex. To minimize the interference from certain metal ions, 0.1 mL of potassium sodium

tartrate solution was added into the test solutions before the color reagent.

Nessler's reagent was prepared as follows: 3.5 g of potassium iodide (KI) and 5.0 g of mercury iodide (HgI_2) were dissolved in 15 mL of ultrapure water to obtain solution A, and 8.0 g of NaOH was dissolved into 25 mL of ultrapure water to obtain solution B. Following that, solution A was slowly mixed with solution B under magnetic stirring. The obtained mixed solution was then diluted to 50 mL with ultrapure water and allowed to stand for one day. Finally, the supernatant in the mixed solution was collected for use.

For the determination of $\text{NH}_3\text{-N}$, a certain volume of the test solution was diluted to fall into the detection range. Subsequently, 0.1 mL of sodium potassium tartrate solution (500 g L^{-1}) and 0.1 mL of Nessler's reagent were successively added to 5 mL of the diluted test solution. The mixed solution was sonicated and then kept standing for 30 min before its absorbance at 420 nm was measured with a UV-Vis spectrophotometer. The corresponding standard curves and calibration curve are shown in Fig.S4.

2.6. Calculation and DFT Computation

In this work, the NO_2^- removal percentage, NH_3 selectivity, FE, NO_2^- removal amount and Pseudo-first-order kinetic model were obtained according to the following calculation methods.

$$\text{Removal percentage of } \text{NO}_2^- = \frac{([\text{NO}_2^- - \text{N}]_0 - [\text{NO}_2^- - \text{N}]_t)}{[\text{NO}_2^- - \text{N}]_0} \times 100\% \quad (1)$$

$$\text{NH}_3 \text{ Selectivity} = \frac{\Delta[\text{NH}_3 - \text{N}]}{([\text{NO}_2^- - \text{N}]_0 - [\text{NO}_2^- - \text{N}]_t)} \times 100\% \quad (2)$$

$$\text{FE} = F \times \Delta[\text{NH}_3 - \text{N}] \times V \times 6 / (M_N \times Q) \times 100\% \quad (3)$$

$$\text{Absolute removal amount of } \text{NO}_2^- = \frac{([\text{NO}_2^- - \text{N}]_0 - [\text{NO}_2^- - \text{N}]_t)}{V \times (t \times m_{\text{cat}})} \quad (4)$$

A pseudo-first-order kinetic model was used to fit the relationship between $\text{NO}_2\text{-N}$ concentration and catalytic reaction time, as shown below:

$$\frac{[\text{NO}_2^- - \text{N}]_t}{[\text{NO}_2^- - \text{N}]_0} = \exp(-kt) \quad (5)$$

Where $[\text{NO}_2^- - \text{N}]_0$ represents the initial concentration of $\text{NO}_2^- - \text{N}$, and $[\text{NO}_2^- - \text{N}]_t$ is the concentration of $\text{NO}_2^- - \text{N}$ at the reaction time t . $\Delta[\text{NH}_3 - \text{N}]$ represents the difference between $\text{NH}_3\text{-N}$ concentration at the reaction time of t and that at the beginning of the reaction. F is Faraday constant ($96,500\text{ C mol}^{-1}$), M_N is the molar mass of nitrogen element (14 mg mmol^{-1}), Q is the total charge input into the reaction system at the reaction time t , V is the volume of electrolyte solution, m_{cat} is the catalyst load, and k is the rate constant of the pseudo-first-order kinetics model.

The detailed information for DFT calculations were presented in the Supplementary Material.

3. Results and discussion

3.1. Characterization of the electrocatalyst

The XRD pattern of the FeP nanoarrays (Fig. 1a) displays several peaks at 32.7° , 37.1° , 46.2° , 46.9° , 48.3° , 50.3° and 55.3° , corresponding to the (011), (111), (121), (220), (211), (130) and (310) crystal planes of FeP (JCPDS: 71-2262) respectively, indicating the successful synthesis of orthorhombic FeP. SEM and HRTEM were then used to investigate the microstructure and crystal surface composition of

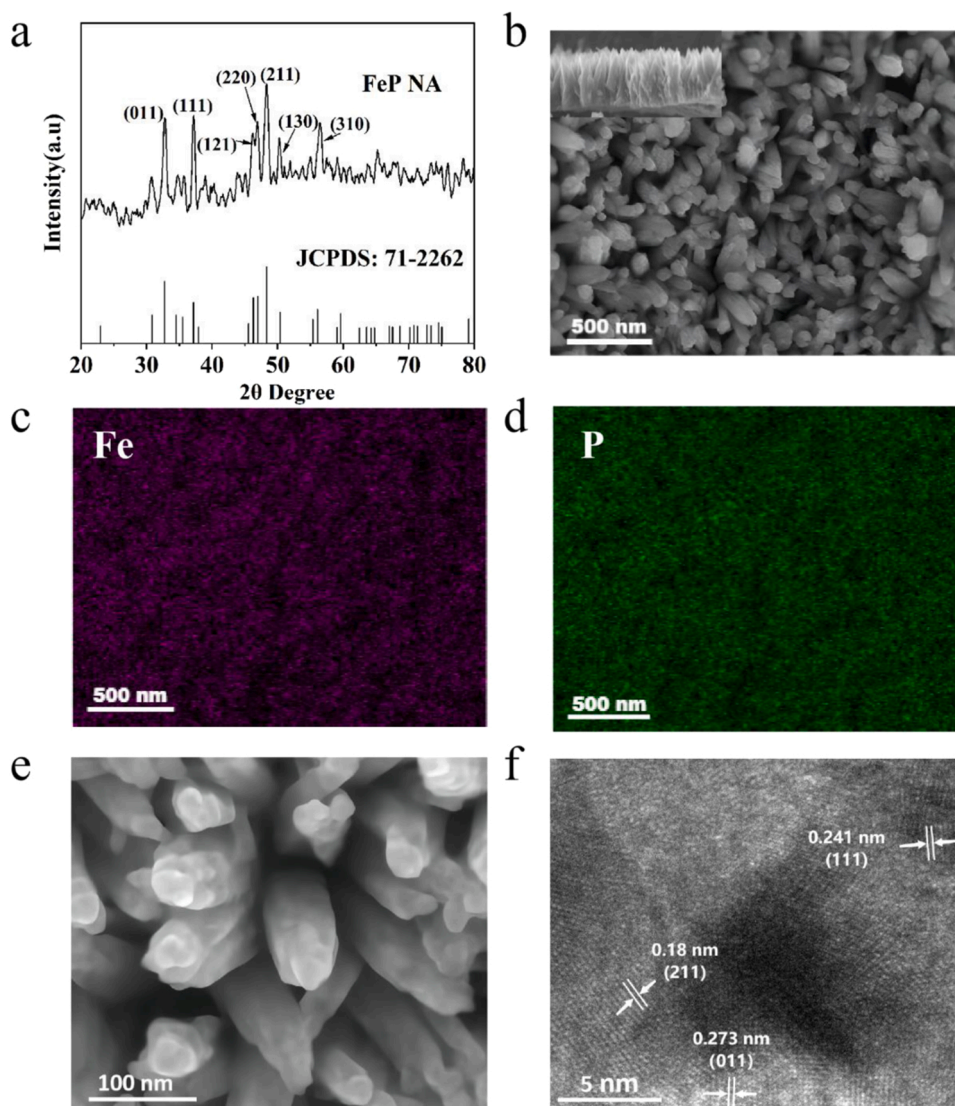


Fig. 1. (a) XRD pattern of FeP nanoarrays scraped from FeP NA|Ti. (b-d) SEM image of FeP NA|Ti and corresponding EDS element mapping images (the inset of b is the side view). (e) SEM image of FeP NA|Ti at higher magnification; (f) HRTEM image of FeP nanoarrays.

the materials. The SEM images of FeP NA|Ti at different magnifications and EDS element mapping images (Fig. 1b-e and Fig.S5) clearly demonstrate that the prepared nanoarrays have a uniform structure with an average diameter of 40–60 nm for the individual nanorods while the distribution of P and Fe elements in the nanoarrays is uniform. A side view of the FeP array (inset of Fig. 1b) clearly shows an array structure. These images indicate that FeP is formed as a highly regular nanoarrays on the Ti substrate. In addition, the HRTEM image of FeP NA|Ti (Fig. 1f) shows clear lattice fringes with lattice spacings of 0.180, 0.241, and 0.273 nm, attributed to the (211), (111), (011) crystal planes of FeP respectively, in accordance with the XRD pattern [44,45].

Next, XPS was conducted to confirm the valence states of the prepared FeP nanoarrays sample. According to a previous reports, the typical $2p_{3/2}$ peak of Fe is situated at a binding energy of 706.8 eV [46]. However, as displayed in Fig. 2a, the Fe 2p peak of FeP is at a slightly higher binding energy which is probably due to the lower valence state of Fe resulting from the weak electron-withdrawing properties of phosphorus. Moreover, the characteristic peak at a binding energy of 707.2 eV suggests that Fe is in an oxidation state

between 0 and 2, indicating the possible presence of a Fe-P bond [45, 47]. Furthermore, the peaks at 710 and 724.2 eV can be attributed to the $2p_{3/2}$ and $2p_{1/2}$ levels of Fe^{2+} , respectively while the peaks at 712.3 and

726.8 eV are attributed to the $2p_{3/2}$ and $2p_{1/2}$ levels of Fe^{3+} , respectively as well as a weak peak at 720.0 eV attributed to a satellite peak [45]. In summary, the XPS spectrum of Fe 2p demonstrated that three valence states of iron ($Fe^{\delta+}$ ($0 < \delta < 2$), Fe^{2+} and Fe^{3+}) exist in the prepared FeP nanoarrays.

Generally, the typical $2p_{3/2}$ peak of P is located at a binding energy of 129.98 eV [46], while that of FeP should be at a slightly lower binding energy because P is more electronegative than Fe. As displayed in Fig. 2b, the peaks at 129.3 and 130.1 eV correspond to the $2p_{3/2}$ and $2p_{1/2}$ levels of $P^{\beta-}$ ($-1 < \beta < 0$) in FeP respectively, and the peak at 133.5 eV indicates the presence of some PO_4^{3-} . The existence of Fe^{3+} and PO_4^{3-} in the samples is probably due to the oxidation of the surface layer of FeP NA|Ti by air, as discussed in previous studies [45,47]. Furthermore, the EDS spectrum (Fig. 2c) demonstrates that the ratio of Fe to P in FeP NA|Ti is 1.08 : 1. The oxygen signal in the EDS is derived from the oxide layer of the Ti substrate and the oxidation product of the surface of the FeP layer [42].

3.2. Electrocatalytic nitrite reduction

3.2.1. Finding the optimal catalytic potential

After the morphology and composition characterization, the

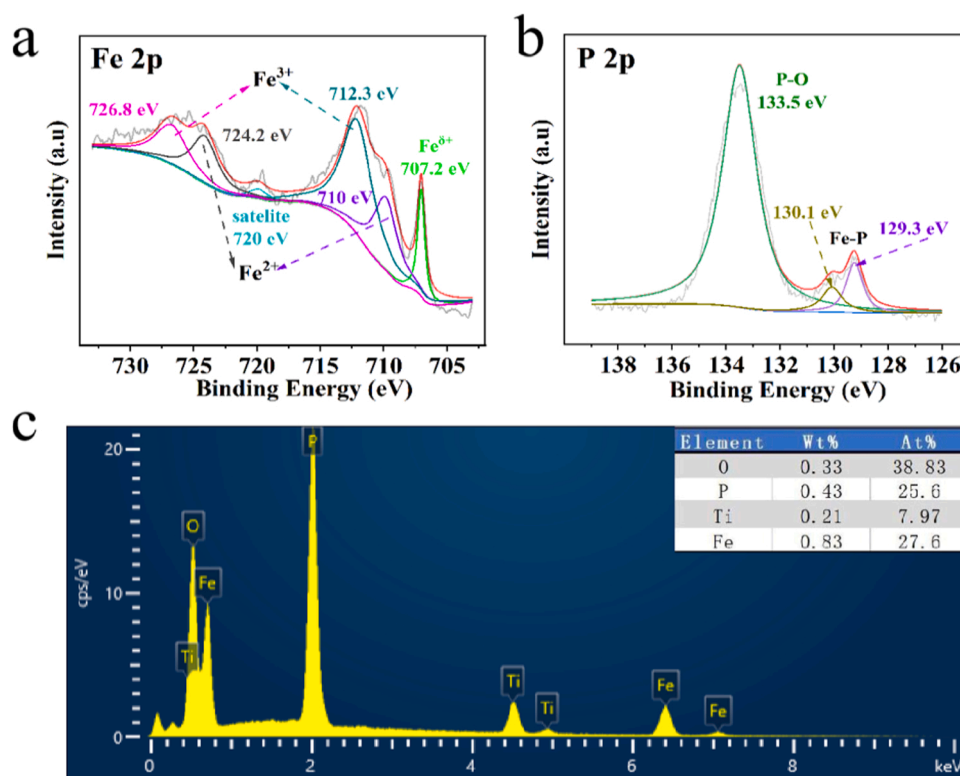


Fig. 2. High resolution XPS spectra of (a) Fe 2p and (b) P 2p in FeP NA/Ti. (c) EDS and element content table of FeP NA/Ti.

electrocatalytic performance of FeP NA/Ti for NO_2^- reduction was evaluated and displayed in Fig. 3. Firstly, the electrochemical behavior of NO_2^- reduction under different applied potentials was studied because the applied potential may greatly influence the distribution of reduction

products and the FE of the reduction reaction [36]. As shown in Fig. 3a, linear sweep voltammetry (LSV) recorded in 0.05 M Na_2SO_4 without (black curve) and with 200 ppm NO_2^- -N (red curve) were obtained at FeP NA/Ti within a potential window of 0.35 to -0.80 V (vs RHE). It is

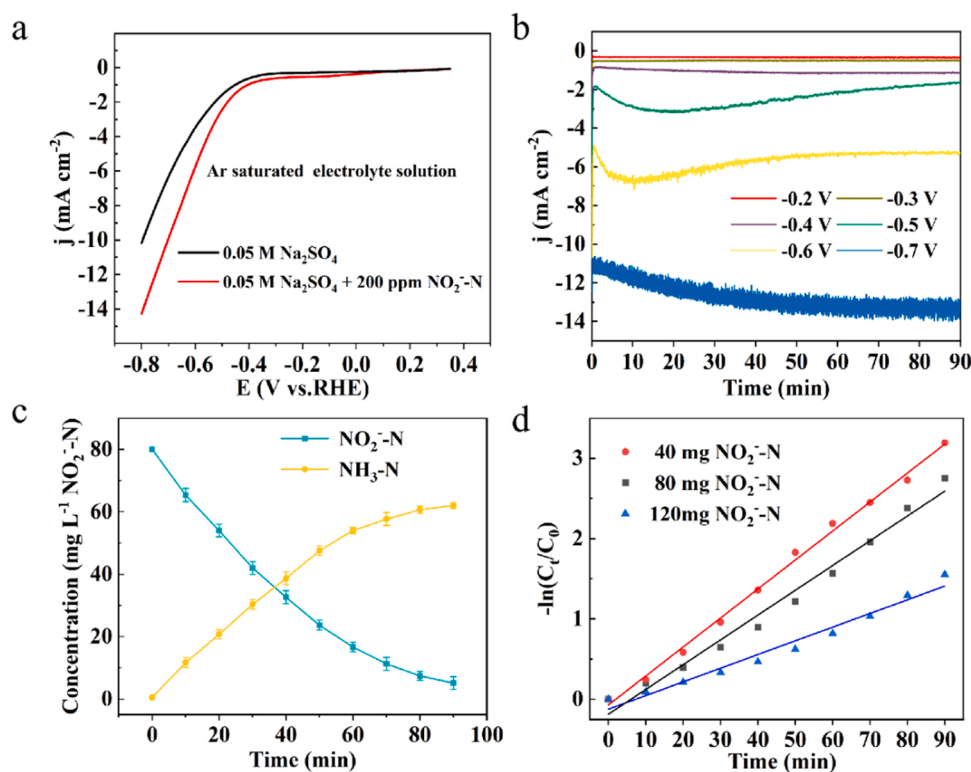


Fig. 3. (a) LSV curves of FeP NA/Ti in 0.05 M Na_2SO_4 (Ar saturated) with/without 200 ppm NO_2^- -N. (b) i-t curves of FeP NA/Ti. (c) Concentration monitoring chart of NO_2^- -N and NH_3 -N during the reaction. (d) Pseudo-first-order kinetic model for electrocatalytic NO_2^- reduction at FeP NA/Ti.

observed that the latter exhibits an obviously larger reduction current density than the former, indicating the significant catalytic activity of FeP NA|Ti for NO_2^- reduction. In the presence of NO_2^- , when the potential was scanned negatively to 0.05 V, the cathodic current started to increase and the maximum change appeared in the potential range of -0.4 to -0.8 V, which is thus regarded as the suitable potential window for the electrocatalytic reduction of NO_2^- .

Next, Fig. 3b displays the chronoamperometry (i-t) curves at different applied potentials. The current curves are relatively smooth at -0.2 , -0.3 and -0.4 V, probably due to the insufficient reactivity of FeP catalyst at low potentials, which resulted in a relatively stable catalyst interface. However, the i-t curves began to fluctuate as the applied potential was further decreased to -0.5 V, and the fluctuation became more intense at -0.7 V, mainly because the low reduction potentials led to initiation of the HER, and the accumulated H_2 bubbles caused fluctuations in the i-t curves at the catalyst interface [36]. More importantly, as also shown in Fig. 3b, the current density at an applied potential of -0.5 V gradually decreased with reaction time after it rapidly reached a steady state after 15 min, implying that the electrocatalytic reduction of NO_2^- has been significantly initiated at -0.5 V and that the reaction rate is highly correlated with the concentration of NO_2^- . To verify this, the concentrations of both NO_2^- and NH_3 in the reaction process were measured at -0.5 V with a time interval of ten minutes. As indicated by Fig. 3c, the NO_2^- concentration decreased while the NH_3 concentration increased with increased reaction time, which slowed down the reduction reaction rate, and thus decreased the cathodic current. This demonstrates that the reduction current is positively correlated with the concentration of NO_2^- , and the kinetics of NO_2^- reduction is consistent with a pseudo-first-order kinetic model (Fig. 3d) [48].

Moreover, Fig. 4a demonstrates the removal percentage of NO_2^- , NH_3 selectivity and FE at different applied potentials. Specifically, as the applied potential was decreased from -0.2 to -0.5 V, both the removal percentage of NO_2^- and NH_3 selectivity exhibited a sharp enhancement from $\sim 5\%$ to $\sim 86\%$ and from $\sim 3.5\%$ to $\sim 80\%$, respectively. This is because the amount of atomic H^* could be enhanced on the catalyst

surface with the decrease in applied potential, which significantly accelerated the hydrogenation reduction of NO_2^- to produce more NH_3 [41]. However, with a further decrease of the applied potential from -0.5 to -0.7 V, the enhancement of both NO_2^- removal percentage and NH_3 selectivity weakened, and the FE also significantly decreased. This could be attributed to the production of a large amount of H_2 evolving from the catalyst surface due to the existence of plentiful atomic H^* [36, 49]. The UV-Vis absorption spectra of the residual NO_2^- (Fig. 4b) and reduction product NH_3 (Fig. S6a) strongly supported the conclusion from Fig. 4a. In addition, N_2H_4 was not detected under different applied potentials (Fig. S6b), which further confirms the high selectivity of the reduction of NO_2^- at FeP NA|Ti. Based on the above discussion, an optimum potential of -0.5 V was applied in the subsequent electrocatalytic tests.

3.2.2. Effect of initial NO_2^- Concentration

Recently, it has been reported that the concentration of NO_2^- impacts the catalytic rate and selectivity during the chemical reduction of NO_2^- by H_2 that is catalyzed by Pd [41]. Therefore, the influence of NO_2^- concentration on the electrocatalytic reduction of NO_2^- was studied using FeP NA|Ti as the working electrode at -0.5 V. With the stepwise increase of NO_2^- -N concentration, both the removal percentage of NO_2^- and NH_3 selectivity obviously declined (Fig. 4c) (the corresponding UV-Vis absorption spectra and i-t curves are shown in Fig. S7a-c), which is consistent with the previous studies [50,51]. Nevertheless, the absolute removal amount of NO_2^- significantly increased with the increase of NO_2^- -N concentration even to a relative high concentration of 200 mg L^{-1} , implying the effectiveness and usability of the prepared FeP NA|Ti for the catalytic reduction of high NO_2^- -N concentrations (Fig. S7d). The reason for the above results could be attributed to the decline of the H^*/NO_2^- ratio on the catalyst surface with the increase of NO_2^- -N concentration. More specifically, at low H^*/NO_2^- ratios, the low amount of H^* could limit the hydrogenation of the excessive concentration of NO_2^- in solution, which may directly react with the reduction intermediates of NO_2^- on the catalyst surface to produce a series of side reactions [41,50]. These reactions would reduce the removal percentage

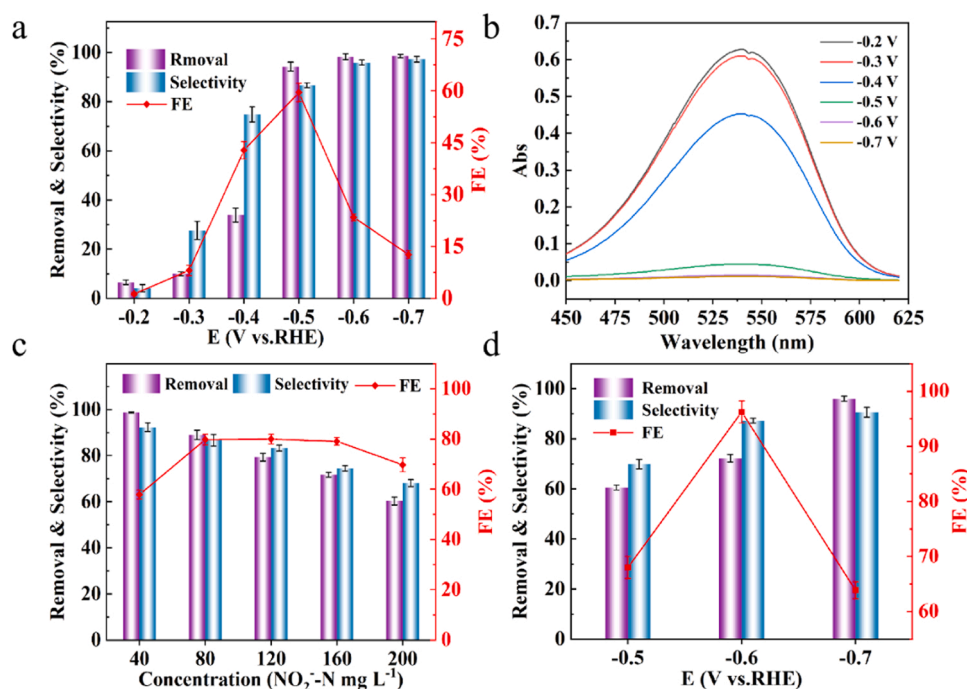


Fig. 4. (a) NO_2^- -N removal percentage, NH_3 selectivity and FE at different applied potentials for reducing 40 mg L^{-1} NO_2^- -N simulated wastewater; (b) The corresponding UV-Vis absorption spectra of residual NO_2^- after dilution of 200 times; NO_2^- -N removal percentage, NH_3 selectivity and FE determined (c) in increasing NO_2^- -N concentrations at -0.5 V and (d) at different potentials in 200 mg L^{-1} NO_2^- -N.

and selectivity of NO_2 to NH_3 [50]. However, although the increase of NO_2 -N concentration resulted in a decline of NO_2 removal percentage and NH_3 selectivity, the absolute removal amount of NO_2 increased which is important for practical applications.

As also indicated by the red curves in Fig. 4c, the FE shows an increasing trend as the NO_2 -N concentration was increased from 40 to 80 mg L^{-1} . Then, the FE plateaued between 80 and 160 mg L^{-1} of NO_2 -N. Following that, the FE significantly decreased when the concentration of NO_2 -N is higher than 160 mg L^{-1} . The above phenomena could be ascribed to the variation of the H^+/NO_2 ratio with increasing NO_2 -N concentrations [41,50]. Specifically, when the NO_2 -N concentration is low (40–80 mg L^{-1}), the amount of atomic H^* produced at -0.5 V is larger relative to NO_2 . Therefore, the HER caused by the excessive atomic H^* could be restrained because of the fast reduction of NO_2 -N by atomic H^* , which is conducive to enhancing the FE. Next, in the higher NO_2 -N concentration range of 80–160 mg L^{-1} , the FE tended to decrease due to the side reactions at the catalyst interface between NO_2 and its reduction intermediate [41]. Meanwhile, the higher concentration of NO_2 -N could react with more atomic H^* to inhibit the HER, thus resulting in an increase of the FE. Consequently, the simultaneous occurrence of these two opposing effects led to a minor change of FE within the 80–160 mg L^{-1} concentration range of NO_2 -N. With the further increase of NO_2 -N concentration from 160 to 200 mg L^{-1} , the excessively high NO_2 concentration caused strong side reactions, and the inhibitory effect on the HER was nearly saturated, both of which accounted for the significant decline of the FE.

To further confirm the above conclusions, we investigated the influence of the H^* amount on the electrocatalytic reduction of NO_2 by changing the H^+/NO_2 ratio by altering the applied potential. This is feasible because H^* is usually generated at the catalyst interface by the electrochemical reduction of H_2O under neutral and alkaline conditions [49]. During the test, the NO_2 -N concentration was fixed at 200 mg L^{-1} , the amount of H^* would increase with the decrease in reduction potentials from -0.5 to -0.7 V. With an increase of the H^+/NO_2 ratio, we assumed that the electrocatalytic reduction of NO_2 should follow three stages elaborated below: (i) In the relatively low ratio range of H^+/NO_2 , the relatively high concentration of NO_2 in the solution cannot be depleted quickly by the insufficient concentration of atomic H^* . Therefore, there would be a strong side reaction between NO_2 and its reduction intermediates on the catalyst surface, resulting in relatively poor NH_3 selectivity, NO_2 removal percentage and FE; (ii) In a moderate ratio range of H^+/NO_2 , the NH_3 selectivity, NO_2 removal percentage and FE would be significantly improved owing to the faster conversion of NO_2 to NH_3 by the larger amount of atomic H^* at the electrode surface; (iii) The highest reaction rate and NH_3 selectivity would be achieved at high H^+/NO_2 ratios with excessive atomic H^* , which however could lead to more HER and lower FE [36].

Encouragingly, the experimental results support the above hypothesis of a three-stage mechanism, as suggested by Fig. 4d. When the applied potential was decreased from -0.5 to -0.6 V, the removal percentage of NO_2 , NH_3 selectivity and FE increased from $\sim 60\%$, $\sim 69\%$ and $\sim 60\%$ to $\sim 72\%$, $\sim 87\%$ and $\sim 96\%$, respectively. As the reduction potential was further decreased to -0.7 V, the NO_2 removal percentage and NH_3 selectivity were enhanced to $\sim 96\%$ and $\sim 90\%$, while the FE was decreased to $\sim 63\%$. The above results could be attributed to the increase in atomic H^* concentration upon the decrease of applied reduction potentials [49]. However, the influence of atomic H^* on the NH_3 selectivity and NO_2 removal percentage was saturated at the reduction potential of -0.6 V, and the FE reached its highest value. A further increase in reduction potential could still improve the NO_2 removal percentage and NH_3 selectivity, however it would also result in severe hydrogen evolution and reduce the FE.

To further identify the role of H^* in the electrocatalytic reduction of NO_2 , a comparative test was conducted using tert-Butanol (TBA) as a scavenger of H^* in the electrocatalytic process [52]. Fig. S8 shows the performance comparison between FeP NA/Ti in 200 mg L^{-1} NO_2 -N and

that in 200 mg L^{-1} NO_2 -N + 40 mM TBA at two applied potentials (-0.5 and -0.6 V). The results demonstrated that the introduction of TBA significantly decreased the removal percentage of NO_2 , NH_3 selectivity and FE because TBA reduced the H^* concentration, indicating that H^* plays an important role in the hydrogenation process during the reduction of NO_2 .

3.2.3. Effect of initial solution pH

It has been reported that the pH environment also impacts the performance of nitrite reduction catalysts. For example, the pH of the NO_2 solution directly affected the NO_2 and H^* coverage of a noble metal catalyst surface during the chemical reduction of NO_2 by H_2 , thus imposing a significant influence on the catalytic performance [53]. In addition, the microbial treatment of nitrate wastewater mainly works in neutral and weak acid/alkali environment, but cannot survive in strong acid and alkali solutions [54]. Herein, we studied the catalytic performance of FeP NA/Ti in NO_2 wastewater samples with increasing pH values from 3 to 11, as shown in Fig. 5a (the corresponding i-t curves and UV-Vis absorption spectra are presented as Fig. S9). The FE curve shows a "volcano" shape with increased pH values, where the highest FE was achieved in neutral conditions, and low FE values were obtained in strong acid and alkali environments. Similarly, the best selectivity also appeared under neutral conditions, showing that the catalyst had the best catalytic performance in a neutral environment, and the weak acid and base had little influence on performance. Different from the FE and selectivity, the removal percentage of NO_2 decreased from 100 % (pH = 3) to $\sim 59\%$ (pH = 11) with the increase of pH. The above results can be attributed to the fact that the speciation of NO_2 is greatly affected by the pH of the solution. In the solution with a pH lower than 3.25, the main form of NO_2 is HNO_2 , while at pH values higher than 3.25, NO_2 is the main species [16]. As an active chemical substance, HNO_2 is readily decomposed at room temperature to produce by-products such as NO_2 and NO [16], resulting in a significant decline in NH_3 selectivity and FE under strong acid conditions. Although the NO_2 removal percentage reached 100 % at pH = 3, the NO_2 and NO generated in this process are strictly controlled atmospheric pollutants, therefore it is not advisable to promote NO_2 reduction by lowering the pH. Meanwhile, the NO_2 removal percentage, NH_3 selectivity and FE obviously decreased when the pH of the system is more than 9. This is probably because the reduction of NO_2 requires a large amount of atomic H^* , which is generated by the adsorption of H_2O in aqueous solution on the surface of the catalyst [49]. The high OH^- concentration in strong alkaline solution significantly reduced the H^+/NO_2 ratio on the catalyst surface, which thus resulted in the low removal percentage of NO_2 , NH_3 selectivity and FE.

3.2.4. Effect of reaction temperature

Temperature has a great influence on chemical reaction rates, especially for biological

wastewater treatment. Low temperature inhibits microbial activity, therefore biological wastewater treatment usually suffers from poor efficiency at low temperature, and even cannot be used [54]. Many places in the world are cold in winter, therefore it is of great practical significance to test the reliability of the electrocatalytic treatment of nitrite wastewater at relatively low temperatures. Fig. 5b displays the treatment efficiency for 80 mg L^{-1} of NO_2 -N at FeP NA/Ti under an applied potential of -0.5 V in the 5–45 $^{\circ}\text{C}$ temperature range. The corresponding i-t curves and UV-Vis absorption spectra are provided in Fig. S10 to verify the authenticity of the data in Fig. 5b. As shown in the Fig. 5b, the NO_2 removal percentage increases with the increase of temperature, and this trend is particularly obvious below 25 $^{\circ}\text{C}$. Even at a low temperature of 5 $^{\circ}\text{C}$, the removal percentage of NO_2 and FE still reached $\sim 71\%$ and $\sim 67\%$, which are only $\sim 17\%$ and $\sim 18\%$ lower than those at room temperature, respectively. Under these conditions, the removal efficiency of NO_2 by microbial treatment can be reduced by up to 5–10 times [54]. Meanwhile, the selectivity only showed a small

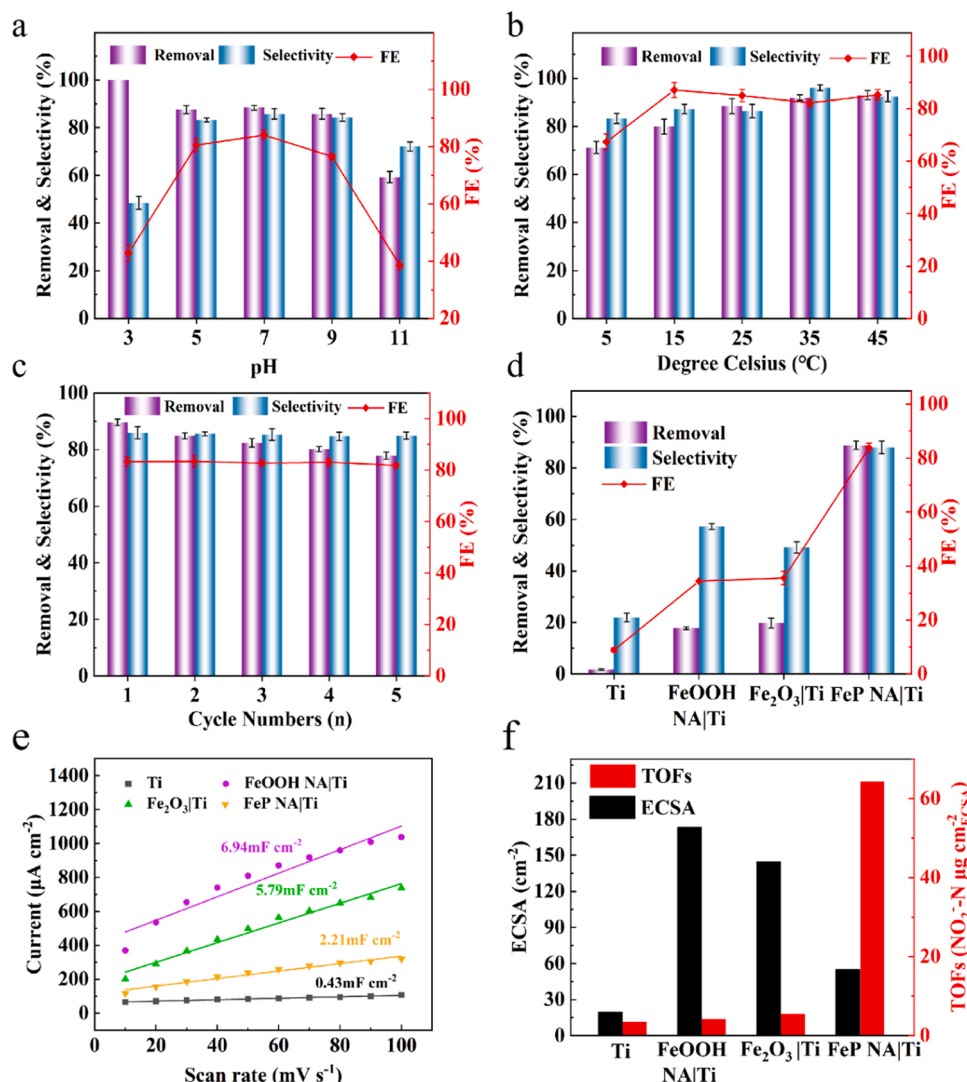


Fig. 5. NO₂-N removal percentage, NH₃ selectivity and FE determined at different (a) pH; (b) initial constant temperature; (c) cycle numbers; and (d) electrode materials. (e): Relationship between current density and CV scan rates for different electrode materials; (f): ECSA and TOFs of different electrode materials.

change, which suggests good temperature adaptability of using FeP NA/Ti for the electrocatalytic treatment of NO₂.

3.2.5. Long-term stability

In practical applications, besides catalytic performance, stability is also one of the most important indicators to evaluate the practicality of a catalytic process. To investigate the stability of the prepared electrocatalyst, five consecutive tests were carried out for electrochemically reducing 80 mg L⁻¹ of NO₂-N simulated wastewater at FeP NA/Ti with an applied potential of -0.5 V for 90 min where Fig. 5c shows the NO₂ removal percentage, NH₃ selectivity and FE at the same FeP NA/Ti obtained after each cycle of the test. The corresponding i-t curves and UV-Vis absorption spectra are shown in Fig. S11 to support Fig. 5c. The results of the stability test show that the FE and NH₃ selectivity remained high except for a small reduction in NO₂ removal percentage (from ~89 % to ~78 %) after 5 cycles, indicating good stability of the FeP catalyst. After the stability test, the SEM images, TEM images and XPS spectra of FeP NA/Ti were collected as Fig. S12. It can be seen from SEM (Fig. S12a, b) and XPS (Fig. S12e, f) that the morphology and composition of FeP have changed, while the lattice of FeP is still observed by TEM (Fig. S12c, d).

3.2.6. Comparison with other materials

Furthermore, the performance of NO₂ reduction at a Ti sheet, FeOOH NA/Ti, Fe₂O₃/Ti and FeP NA/Ti was compared to demonstrate the effectiveness of FeP for the electrocatalytic reduction of NO₂ in 80 mg L⁻¹ of NO₂-N simulated wastewater under an applied potential of -0.5 V. As displayed in Fig. 5d, the removal percentage of NO₂ at a Ti sheet is negligible, indicating that Ti has no impact on NO₂ electrocatalytic reduction. Compared with the Ti sheet, FeOOH NA/Ti exhibited a stronger capability for catalytic reduction of NO₂ (~18 % removal percentage, ~57 % selectivity and ~34 % FE), which is quite similar to Fe₂O₃/Ti (~20 % removal percentage, ~49 % selectivity and ~35 % FE). More importantly, FeP NA/Ti showed the highest removal percentage of NO₂ (~89 %), NH₃ selectivity (~88 %) and FE (~83 %) among all the electrodes, confirming that the most efficient electrocatalyst for NO₂ reduction is FeP among all the studied materials. The corresponding i-t curves and UV-Vis absorption spectra are provided as Fig. S13 to verify the authenticity of Fig. 5d. To further verify the activity of FeP NA/Ti, the double layer capacitances (C_{dl}) of different materials (Fig. S14 a-d) were measured by cyclic voltammetry (CV) at increasing sweep rates from 10 to 100 mV s⁻¹, and the electrochemical active surface (ECSA) of these materials were calculated based on the methods presented in the Supplementary material [55]. As shown in Fig. 5e, f and Table S1, FeP NA/Ti exhibits the largest conversion

(64.3 $\mu\text{g NO}_2\text{-N cm}^{-2}_{\text{ECSA}}$) among all the prepared materials although its ESCA is not the largest one, further confirming the high catalytic activity of FeP NA|Ti.

3.2.7. Nitrogen source verification

To confirm that NH_4^+ was transformed from NO_2 by electrocatalytic reduction, comparative tests were conducted in (i) 0.05 M Na_2SO_4 containing 80 mg L^{-1} $\text{NO}_2\text{-N}$ at -0.5 V, (ii) 0.05 M Na_2SO_4 at -0.5 V, and (iii) 0.05 M Na_2SO_4 containing 80 mg L^{-1} $\text{NO}_2\text{-N}$ at open circuit potential. The results (Fig. S15) show that $\text{NH}_3\text{-N}$ can only be produced from NO_2 at a suitable applied potential of -0.5 V. To further verify the source of the reaction product $\text{NH}_3\text{-N}$, we used $\text{Na}^{15}\text{NO}_2$ as the isotope nitrogen source to conduct a $^{15}\text{NO}_2$ reduction test [56]. As shown in Fig. S16, when $^{15}\text{NO}_2$ was used as the nitrogen source, the double peaks of $^{15}\text{NH}_4^+$ at 6.89 and 7.04 ppm were detected in the reduction product, while the triple peaks of $^{14}\text{NH}_4^+$ at 6.86, 6.97 and 7.07 ppm were observed with $^{14}\text{NO}_2$ as the nitrogen source. Using maleic acid as a standard substance for quantitative analysis, the concentration of $^{15}\text{NH}_4^+\text{-N}$ determined by ^1H NMR was very close to that measured by the UV-Vis method, demonstrating that $\text{NH}_3\text{-N}$ in the product was completely derived from $\text{NO}_2\text{-N}$.

3.3. Mechanism exploration

In order to further explore the reaction mechanism, *in situ* ATR-FTIR and DFT calculations were carried out. The intermediates on the catalyst surface during the electrocatalytic reduction reaction were determined by *in situ* ATR-FTIR. As shown in Fig. S17a, the IR signal at 1256 and 1336 cm^{-1} are attributed to the asymmetric stretching and symmetric stretching mode of $^*\text{NO}_2$, respectively [57,58]. The absorption bands at 1464 and 1616 cm^{-1} can be ascribed to the bending mode of $\sigma(\text{N-H})$ in $(^*\text{NH}_x)_{\text{ads}}$ and stretching mode of $^*\text{NO}_{\text{ads}}$, respectively [59,60]. The interference of an H_2O absorption peak at ~ 1600 cm^{-1} can be avoided by using D_2O as the solvent. As shown in Fig. S17b, the absorption peak at 1614 cm^{-1} is attributed to the stretching mode of $^*\text{NO}_{\text{ads}}$. Furthermore, the ATR-FTIR spectrum of a 0.1 M NaNO_2 solution (Fig. S17c) confirms that the absorption peaks at 1250 and 1340 cm^{-1} are attributed to the asymmetric stretching and symmetric stretching modes of NO_2 , respectively. The above results suggest the existence of $^*\text{NO}$ and $^*\text{NH}_x$ adsorption intermediates during the process of NO_2 catalytic reduction. Based on this result, DFT calculations were then conducted to further investigate the mechanism of nitrite conversion on the FeP catalyst in a more specific way. The calculated lattice parameter of FeP agrees well with previous reports [61]. Based on the experimental

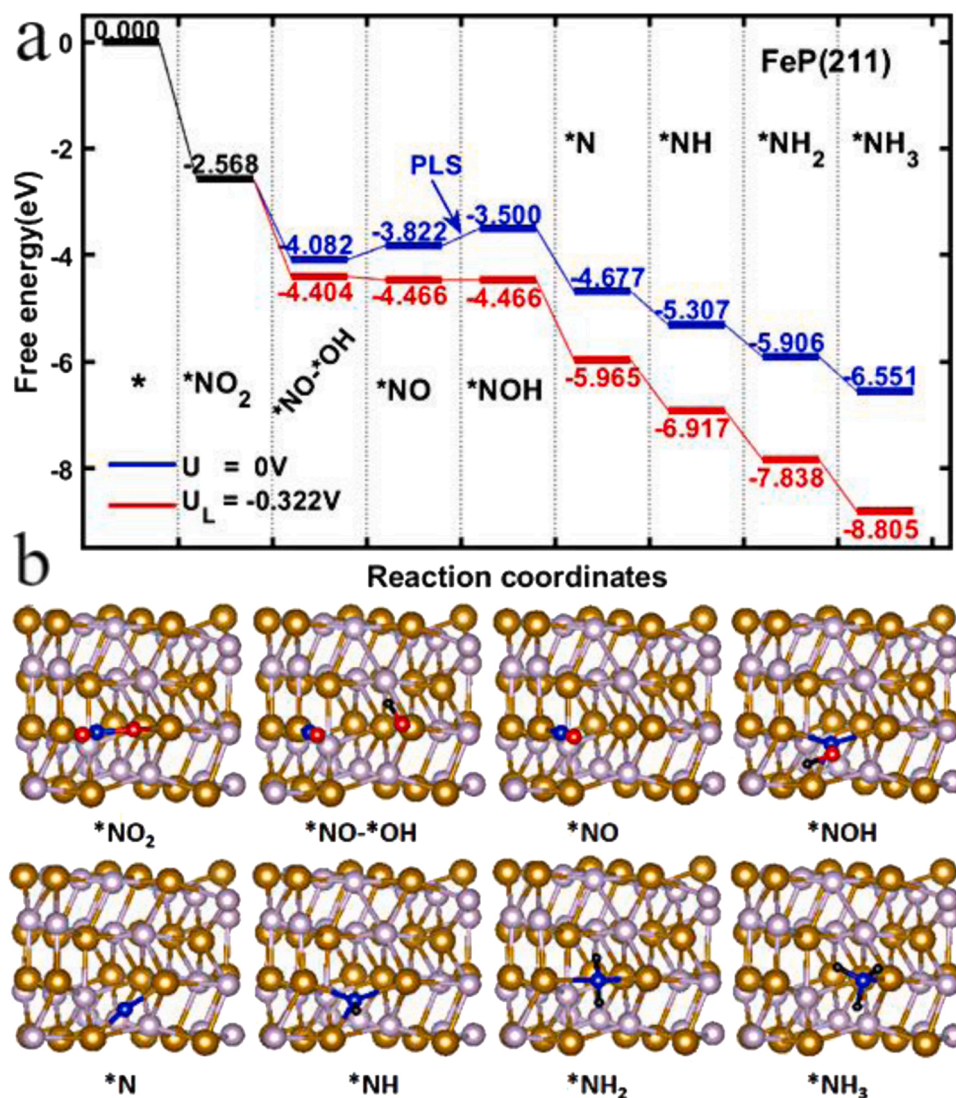


Fig. 6. (a): Free energy diagram of NO_2RR on FeP (211) surface, starting from $^*\text{NO}_2$ in Fig. S16a; (b): configurations of different intermediates during NO_2 reduction reaction process on FeP (211) surface. Bronze, light purple, blue, red and black spheres represent Fe, P, N, O and H atoms, respectively.

characterization, we picked three model surfaces which are (211) and (111) and (011). A density of states (DOS) analysis of these facets was conducted and is shown in Fig.S18 to S20. It is clear that abundant states exist across the Fermi level which indicates their excellent conductivity. The (211) facet was used here as an example because it exhibited the highest peak in the XRD pattern. NO₂ adsorption is the first yet crucial step for the whole reduction process, so different adsorption configurations were calculated and compared on FeP (211). Three configurations with the lowest adsorption energies are depicted in Fig. S21. It can be seen that NO₂ tends to be adsorbed in an associative way as suggested by previous work [36], which means one nitrogen and one oxygen atoms bonds with adjacent iron atoms separately. The P sites were also tested but they were found to be incapable of adsorbing an NO₂ ion. The lowest NO₂ adsorption free energy on FeP (211) reaches −2.57 eV which indicates decent adsorption properties to enable further reduction. The nitrite reduction mechanism was determined to be continuous hydrogenation (*NO₂ → *NOOH → *NO → *NOH → *N → *NH → *NH₂ → *NH₃) which has also been reported by previous studies [36,39,62]. Along this pathway, the free energy diagram under different external potentials and atomic configurations of all intermediates are shown in Fig. 6. After the stable adsorption of NO₂ with a free energy release of −2.57 eV, the first hydrogenation step is exothermic with a negative ΔG of −1.51 eV, followed by the only two endothermic steps during the whole reaction. It is worth noting that the potential limiting step (PLS) is identified as the hydrogenation of *NO (*NO + H⁺ + e[−] → *NOH), which is consistent with previous works [36], and the free energy change is only 0.32 eV.

Additionally, we also performed DFT calculations for FeP (011) and FeP (111) because they also exhibit substantial peaks in the XRD pattern. The (√2 × √2) plane was picked for both surfaces because we wish to exclude the mirror interactions from adjacent cells. Similar to FeP (211), NO₂ adsorbs strongly on both surfaces via the associative pattern (Fig. S22 and S24), and the PLS is confirmed to be the same (*NO + H⁺ + e[−] → *NOH). However, the largest ΔG change varies as can be seen in Fig. S23 and S25: the most uphill free energy change on FeP (011) is 0.33 eV, which is close to that of FeP (211), suggesting high catalytic activity on the (011) surface. On the other hand, FeP (111) has the largest ΔG change of 0.77 eV and is regarded to be poorly active for NO₂ reduction. Considering that FeP (211) and FeP (011) are the two strongest planes observed in the XRD characterization, our calculation is in accordance with the excellent performance observed in the experiments.

4. Conclusion

In this work, FeP NA|Ti was prepared, characterized, and demonstrated to be an efficient electrocatalyst for the conversion of nitrite to ammonia. The influence of applied potential, NO₂-N concentration, pH and temperature on the electrocatalytic performance of FeP NA|Ti was studied in detail. Specifically, −0.5 V vs RHE was determined to be the optimum reduction potential considering the balance between the performance and the interface stability of the catalyst. Although the NO₂ removal percentage and NH₃ selectivity declined with an increase in NO₂-N concentration, the absolute removal amount increased. The pH study indicated that the electrocatalyst had the best catalytic performance in a neutral environment, and the presence of a weak acid or base had little influence on the catalytic performance. Moreover, within a temperature range of 5–45 °C, there was little impact on the performance of FeP, implying good temperature applicability under practical conditions. Most of the above results could be explained by the variation of H⁺/NO₂ ratio with the experimental conditions. Finally, DFT calculations confirmed that NO₂ reduction mainly occurred on the (011) and (211) facet of FeP and the potential limiting step was “*NO + H⁺ + e[−] → *NOH”. This work demonstrated that FeP is a highly efficient catalyst with low cost for both eliminating and recycling nitrite in water.

CRediT authorship contribution statement

Jiangfeng Yuan: Conceptualization, Formal analysis, Investigation, Data curation Writing – original draft, Writing – review & editing, Visualization. **(Hanqing Yin):** Software, Methodology, Writing – review & editing. **Xiaoxin Jin:** Validation. **Dan Zhao:** Methodology. **Yuan Liu:** Investigation. **Aijun Du:** Software, Writing – review & editing. **Xiaoqiang Liu:** Conceptualization, Resources, Writing – original draft, Writing – review & editing, Supervision, Project administration, Funding acquisition. **Anthony P. O’Mullane:** Writing – review & editing, Software, Conceptualization.

Declaration of Competing Interest

The authors declare the following financial interests/personal relationships which may be considered as potential competing interests: Xiaoqiang Liu reports financial support was provided by National Natural Science Foundation of China.

Data Availability

Data will be made available on request.

Acknowledgement

This work was financially supported by the National Natural Science Foundation of China (No. 62071169).

Appendix A. Supporting information

Supplementary data associated with this article can be found in the online version at doi:10.1016/j.apcatb.2022.122353.

References

- [1] S. Radhakrishnan, K. Krishnamoorthy, C. Sekar, J. Wilson, S.J. Kim, A highly sensitive electrochemical sensor for nitrite detection based on Fe₂O₃ nanoparticles decorated reduced graphene oxide nanosheets, *Appl. Catal. B* 148–149 (2014) 22–28, <https://doi.org/10.1016/j.apcatb.2013.10.044>.
- [2] B.M. Jayawardane, S. Wei, I.D. McKelvie, S.D. Kolev, Microfluidic paper-based analytical device for the determination of nitrite and nitrate, *Anal. Chem.* 86 (2014) 7274–7279, <https://doi.org/10.1021/ac5013249>.
- [3] N. Gruber, J.N. Galloway, An Earth-system perspective of the global nitrogen cycle, *Nature* 451 (2008) 293–296, <https://doi.org/10.1038/nature06592>.
- [4] D.E. Canfield, A.N. Glazer, P.G. Falkowski, The evolution and future of earth’s nitrogen cycle, *Science* 330 (2010) 192–196, <https://doi.org/10.1126/science.1186120>.
- [5] J.K. Chinthaginjala, L. Lefferts, Support effect on selectivity of nitrite reduction in water, *Appl. Catal. B* 101 (2010) 144–149, <https://doi.org/10.1016/j.apcatb.2010.09.023>.
- [6] H. Li, C. Yan, H. Guo, K. Shin, S.M. Humphrey, C.J. Werth, G. Henkelman, Cu₂Ir_{1-x} nanoalloy catalysts achieve near 100% selectivity for aqueous nitrite reduction to NH₃, *ACS Catal.* 10 (2020) 7915–7921, <https://doi.org/10.1021/acscatal.0c01604>.
- [7] I. Dodouche, F. Epron, Promoting effect of electroactive polymer supports on the catalytic performances of palladium-based catalysts for nitrite reduction in water, *Appl. Catal. B* 76 (2007) 291–299, <https://doi.org/10.1016/j.apcatb.2007.06.002>.
- [8] I.G. Casella, M. Contursi, Highly dispersed rhodium particles on multi-walled carbon nanotubes for the electrochemical reduction of nitrate and nitrite ions in acid medium, *Electrochim. Acta* 138 (2014) 447–453, <https://doi.org/10.1016/j.electacta.2014.05.125>.
- [9] T. Kandemir, M.E. Schuster, A. Senyshyn, M. Behrens, R. Schlögl, The Haber-Bosch process revisited: on the real structure and stability of “ammonia iron” under working conditions, *Angew. Chem. Int. Ed.* 52 (2013) 12723–12726, <https://doi.org/10.1002/anie.201305812>.
- [10] J. Erisman, M. Sutton, J. Galloway, et al., How a century of ammonia synthesis changed the world, *Nat. Geosci.* 1 (2008) 636–639, <https://doi.org/10.1038/ngeo325>.
- [11] D. Qi, F. Lv, T. Wei, M. Jin, G. Meng, S. Zhang, Q. Liu, W. Liu, D. Ma, M.S. Hamdy, J. Luo, X. Liu, High-efficiency electrocatalytic NO reduction to NH₃ by nanoporous VN, *Nano Res. Energy* 1 (2022), <https://doi.org/10.26599/nre.2022.9120022>.
- [12] F. Jiao, B. Xu, Electrochemical ammonia synthesis and ammonia fuel cells, *Adv. Mater.* 31 (2019), e1805173, <https://doi.org/10.1002/adma.201805173>.

- [13] C. Smith, A.K. Hill, L. Torrente-Murciano, Current and future role of Haber–Bosch ammonia in a carbon-free energy landscape, *Energ. Environ. Sci.* 13 (2020) 331–344, <https://doi.org/10.1039/c9ee02873k>.
- [14] Y. Zhao, B.P. Setzler, J. Wang, J. Nash, T. Wang, B. Xu, Y. Yan, An efficient direct ammonia fuel cell for affordable carbon-neutral transportation, *Joule* 3 (2019) 2472–2484, <https://doi.org/10.1016/j.joule.2019.07.005>.
- [15] T. Qin, F. Li, X. Liu, J. Yuan, R. Jiang, Y. Sun, H. Zheng, A.P. O'Mullane, Template-assisted synthesis of high-efficiency bifunctional catalysts with roller-comb-like nanostructure for rechargeable zinc-air batteries, *Chem. Eng. J.* 429 (2022), <https://doi.org/10.1016/j.cej.2021.132199>.
- [16] M.D. Victor Rosca, Matheus T. de Groot, Marc T. M. Koper, Nitrogen cycle electrocatalysis, *Chem. Rev.* 109 (2009) 2209–2244.
- [17] J. Liang, Q. Zhou, T. Mou, H. Chen, L. Yue, Y. Luo, Q. Liu, M.S. Hamdy, A. A. Alshehri, F. Gong, X. Sun, FeP nanorod array: A high-efficiency catalyst for electroreduction of NO to NH₃ under ambient conditions, *Nano Res.* 15 (2022) 4008–4013, <https://doi.org/10.1007/s12274-022-4174-0>.
- [18] Z. Li, J. Liang, Q. Liu, L. Xie, L. Zhang, Y. Ren, L. Yue, N. Li, B. Tang, A.A. Alshehri, M.S. Hamdy, Y. Luo, Q. Kong, X. Sun, High-efficiency ammonia electrosynthesis via selective reduction of nitrate on ZnCo₂O₄ nanosheet array, *Mater. Today Phys.* 23 (2022), <https://doi.org/10.1016/j.mtphys.2022.100619>.
- [19] J. Liang, Q. Liu, A.A. Alshehri, X. Sun, Recent advances in nanostructured heterogeneous catalysts for N-cycle electrocatalysis, *Nano Res. Energy* 1 (2022), <https://doi.org/10.26599/nre.2022.9120010>.
- [20] A.J. Medford, M.C. Hatzell, Photon-driven nitrogen fixation: current progress, thermodynamic considerations, and future outlook, *ACS Catal.* 7 (2017) 2624–2643, <https://doi.org/10.1021/acscatal.7b00439>.
- [21] H. Zheng, S. Zhang, X. Liu, A.P. O'Mullane, The application and improvement of TiO₂ (titanate) based nanomaterials for the photoelectrochemical conversion of CO₂ and N₂ into useful products, *Catal. Sci. Technol.* 11 (2021) 768–778, <https://doi.org/10.1039/d0cy02048f>.
- [22] L.F. Greenlee, J.N. Renner, S.L. Foster, The use of controls for consistent and accurate measurements of electrocatalytic ammonia synthesis from dinitrogen, *ACS Catal.* 8 (2018) 7820–7827, <https://doi.org/10.1021/acscatal.8b02120>.
- [23] Y. Zhao, F. Wu, Y. Miao, C. Zhou, N. Xu, R. Shi, L.Z. Wu, J. Tang, T. Zhang, Revealing ammonia quantification minefield in photo/electrocatalysis, *Angew. Chem. Int. Ed.* 60 (2021) 21728–21731, <https://doi.org/10.1002/anie.202108769>.
- [24] J. Choi, B.H.R. Suryanto, D. Wang, H.L. Du, R.Y. Hodgetts, F.M. Ferrero Vallana, D. R. MacFarlane, A.N. Simonov, Identification and elimination of false positives in electrochemical nitrogen reduction studies, *Nat. Commun.* 11 (2020) 5546, <https://doi.org/10.1038/s41467-020-19130-z>.
- [25] B.H.R. Suryanto, H.-L. Du, D. Wang, J. Chen, A.N. Simonov, D.R. MacFarlane, Challenges and prospects in the catalysis of electroreduction of nitrogen to ammonia, *Nat. Catal.* 2 (2019) 290–296, <https://doi.org/10.1038/s41929-019-0252-4>.
- [26] J. Crawford, H. Yin, A. Du, A.P. O'Mullane, Nitrate-to-Ammonia Conversion at an InSn-Enriched Liquid-Metal Electrode, *Angew. Chem. Int. Ed.* 61 (2022), e202201604, <https://doi.org/10.1002/anie.202201604>.
- [27] A.M. Bergquist, J.K. Choe, T.J. Strathmann, C.J. Werth, Evaluation of a hybrid ion exchange-catalyst treatment technology for nitrate removal from drinking water, *Water Res.* 96 (2016) 177–187, <https://doi.org/10.1016/j.watres.2016.03.054>.
- [28] X. Xu, L. Hu, Z.R. Li, L.S. Xie, S.J. Sun, L.C. Zhang, J. Li, Y.S. Luo, X.D. Yan, M. S. Hamdy, Q.Q. Kong, X.P. Sun, Q. Liu, Oxygen vacancies in Co₃O₄ nanoarrays promote nitrate electroreduction for ammonia synthesis, *Sustain. Energ. Fuels* 6 (2022) 4130–4136, <https://doi.org/10.1039/d2se00830k>.
- [29] Q. Chen, J. Liang, Q. Liu, K. Dong, L. Yue, P. Wei, Y. Luo, Q. Liu, N. Li, B. Tang, A. A. Alshehri, M.S. Hamdy, Z. Jiang, X. Sun, Co nanoparticle-decorated pomelo-peel-derived carbon enabled high-efficiency electrocatalytic nitrate reduction to ammonia, *Chem. Commun.* 58 (2022) 4259–4262, <https://doi.org/10.1039/d2cc00952h>.
- [30] H. Yue, L. Xue, F. Chen, Efficiently electrochemical removal of nitrite contamination with stable RuO₂-TiO₂/Ti electrodes, *Appl. Catal. B* 206 (2017) 683–691, <https://doi.org/10.1016/j.apcatb.2017.02.005>.
- [31] P. Kuntke, M. Rodrigues, T. Sleutels, M. Saakes, H.V.M. Hamelers, C.J.N. Buisman, Energy-efficient ammonia recovery in an up-scaled hydrogen gas recycling electrochemical system, *ACS Sustain. Chem. Eng.* 6 (2018) 7638–7644, <https://doi.org/10.1021/acssuschemeng.8b00457>.
- [32] H. Cruz, Y.Y. Law, J.S. Guest, K. Rabaey, D. Batstone, B. Laycock, W. Verstraete, I. Pikaar, Mainstream ammonium recovery to advance sustainable urban wastewater management, *Environ. Sci. Technol.* 53 (2019) 11066–11079, <https://doi.org/10.1021/acs.est.9b00603>.
- [33] Y. Arikawa, Y. Otsubo, H. Fujino, S. Horiuchi, E. Sakuda, K. Umakoshi, Nitrite reduction cycle on a dinuclear ruthenium complex producing ammonia, *J. Am. Chem. Soc.* 140 (2018) 842–847, <https://doi.org/10.1021/jacs.7b12020>.
- [34] J.R. Stokro, B. Kandemir, E.M. Matson, K.L. Bren, Electrocatalytic multielectron nitrite reduction in water by an iron complex, *ACS Catal.* 10 (2020) 13968–13972, <https://doi.org/10.1021/acscatal.0c03600>.
- [35] S. Xu, H.Y. Kwon, D.C. Ashley, C.H. Chen, E. Jakubikova, J.M. Smith, Intramolecular hydrogen bonding facilitates electrocatalytic reduction of nitrite in aqueous solutions, *Inorg. Chem.* 58 (2019) 9443–9451, <https://doi.org/10.1021/acs.inorgchem.9b01274>.
- [36] J. Liang, B. Deng, Q. Liu, G. Wen, Q. Liu, T. Li, Y. Luo, A.A. Alshehri, K. A. Alzahrani, D. Ma, X. Sun, High-efficiency electrochemical nitrite reduction to ammonium using a Cu₃P nanowire array under ambient conditions, *Green. Chem.* 23 (2021) 5487–5493, <https://doi.org/10.1039/d1gc01614h>.
- [37] C. Wang, W. Zhou, Z. Sun, Y. Wang, B. Zhang, Y. Yu, Integrated selective nitrite reduction to ammonia with tetrahydroisoquinoline semi-dehydrogenation over a vacancy-rich Ni bifunctional electrode, *J. Mater. Chem. A* 9 (2021) 239–243, <https://doi.org/10.1039/d0ta09590g>.
- [38] D. Zhao, J. Liang, J. Li, L. Zhang, K. Dong, L. Yue, Y. Luo, Y. Ren, Q. Liu, M. S. Hamdy, Q. Li, Q. Kong, X. Sun, A. TiO_{2-x} nanobelt array with oxygen vacancies: an efficient electrocatalyst toward nitrite conversion to ammonia, *Chem. Commun.* (2022), <https://doi.org/10.1039/d2cc00856d>.
- [39] G. Wen, J. Liang, L. Zhang, T. Li, Q. Liu, X. An, X. Shi, Y. Liu, S. Gao, A.M. Asiri, Y. Luo, Q. Kong, X. Sun, Ni₂P nanosheet array for high-efficiency electrohydrogenation of nitrite to ammonia at ambient conditions, *J. Colloid Inter. Sci.* 606 (2022) 1055–1063, <https://doi.org/10.1016/j.jcis.2021.08.050>.
- [40] H. Wan, A. Bagger, J. Rossmel, Electrochemical nitric oxide reduction on metal surfaces, *Angew. Chem. Int. Ed.* 60 (2021) 21966–21972, <https://doi.org/10.1002/anie.202108575>.
- [41] H. Shin, S. Jung, S. Bae, W. Lee, H. Kim, Nitrite reduction mechanism on a Pd surface, *Environ. Sci. Technol.* 48 (2014) 12768–12774, <https://doi.org/10.1021/es503772x>.
- [42] P. Jiang, Q. Liu, Y. Liang, J. Tian, A.M. Asiri, X. Sun, A cost-effective 3D hydrogen evolution cathode with high catalytic activity: FeP nanowire array as the active phase, *Angew. Chem. Int. Ed.* 53 (2014) 12855–12859, <https://doi.org/10.1002/anie.201406848>.
- [43] G.W. Watt, J.D. Chrisp, Spectrophotometric method for determination of hydrazine, *Anal. Chem.* 24 (1952) 2006–2008, <https://doi.org/10.1021/ac60072a044>.
- [44] Y. Yu, Z. Peng, M. Asif, H. Wang, W. Wang, Z. Wu, Z. Wang, X. Qiu, H. Tan, H. Liu, FeP nanocrystals embedded in N-doped carbon nanosheets for efficient electrocatalytic hydrogen generation over a broad pH range, *ACS Sustain. Chem. Eng.* 6 (2018) 11587–11594, <https://doi.org/10.1021/acssuschemeng.8b01746>.
- [45] Z. He, N. Zheng, L. Zhang, Y. Tian, Z. Hu, L. Shu, Efficient inactivation of intracellular bacteria in dormant amoeba spores by FeP, *J. Hazard. Mater.* 425 (2022), 127996, <https://doi.org/10.1016/j.jhazmat.2021.127996>.
- [46] C.J. Powell, Recommended auger parameters for 42 elemental solids, *J. Electron Spectrosc.* 185 (2012) 1–3, <https://doi.org/10.1016/j.elspec.2011.12.001>.
- [47] Y. Yu, Z. Peng, M. Asif, H. Wang, W. Wang, Z. Wu, Z. Wang, X. Qiu, H. Tan, H. Liu, FeP nanocrystals embedded in N-doped carbon nanosheets for efficient electrocatalytic hydrogen generation over a broad pH range, *ACS Sustain. Chem. Eng.* 6 (2018) 11587–11594, <https://doi.org/10.1021/acssuschemeng.8b01746>.
- [48] F. Yao, M. Jia, Q. Yang, F. Chen, Y. Zhong, S. Chen, L. He, Z. Pi, K. Hou, D. Wang, X. Li, Highly selective electrochemical nitrate reduction using copper phosphide self-supported copper foam electrode: performance, mechanism, and application, *Water Res.* 193 (2021), 116881, <https://doi.org/10.1016/j.watres.2021.116881>.
- [49] J. Zhu, L. Hu, P. Zhao, L.Y.S. Lee, K.Y. Wong, Recent advances in electrocatalytic hydrogen evolution using nanoparticles, *Chem. Rev.* 120 (2020) 851–918, <https://doi.org/10.1021/acs.chemrev.9b00248>.
- [50] X. Lv, H. Peng, X. Wang, L. Hu, M. Peng, Z. Liu, G. Jiang, Nitrate reduction by nanoscale zero valent iron (nFe⁰)-based systems: mechanism, reaction pathway and strategy for enhanced N₂ formation, *Chem. Eng. J.* 430 (2022), <https://doi.org/10.1016/j.cej.2021.133133>.
- [51] L. Su, K. Li, H. Zhang, M. Fan, D. Ying, T. Sun, Y. Wang, J. Jia, Electrochemical nitrate reduction by using a novel Co₃O₄/Ti cathode, *Water Res.* 120 (2017) 1–11, <https://doi.org/10.1016/j.watres.2017.04.069>.
- [52] J. Gao, B. Jiang, C. Ni, Y. Qi, X. Bi, Enhanced reduction of nitrate by noble metal-free electrocatalysis on P doped three-dimensional Co₃O₄ cathode: Mechanism exploration from both experimental and DFT studies, *Chem. Eng. J.* 382 (2020), <https://doi.org/10.1016/j.cej.2019.123034>.
- [53] C.A. Clark, C.P. Reddy, H. Xu, K.N. Heck, G. Luo, T.P. Senftle, M.S. Wong, Mechanistic insights into pH-controlled nitrite reduction to ammonia and hydrazine over rhodium, *ACS Catal.* 10 (2019) 494–509, <https://doi.org/10.1021/acscatal.9b03239>.
- [54] S.K.M. Hune, E.R. Rene, E.D. van Hullebusch, A.P. Annachhatre, Nitrate removal from groundwater: a review of natural and engineered processes, *J. Water Supply Res. T* 67 (2018) 885–902, <https://doi.org/10.2166/aqua.2018.194>.
- [55] C. Wei, R.R. Rao, J. Peng, B. Huang, I.E.L. Stephens, M. Risch, Z.J. Xu, Y. Shao-Horn, Recommended practices and benchmark activity for hydrogen and oxygen electrocatalysis in water splitting and fuel cells, *Adv. Mater.* 31 (2019), e1806296, <https://doi.org/10.1002/adma.201806296>.
- [56] S.Z. Andersen, V. Colic, S. Yang, J.A. Schwalbe, A.C. Nielander, J.M. McEnaney, K. Enemark-Rasmussen, J.G. Baker, A.R. Singh, B.A. Rohr, M.J. Statt, S.J. Blair, S. Mezzavilla, J. Kibsgaard, P.C.K. Vesborg, M. Cargnello, S.F. Bent, T.F. Jaramillo, I.E.L. Stephens, J.K. Nørskov, I. Chorkendorff, A rigorous electrochemical ammonia synthesis protocol with quantitative isotope measurements, *Nature* 570 (2019) 504–508, <https://doi.org/10.1038/s41586-019-1260-x>.
- [57] M.C. Figueiredo, V. Climent, J.M. Feliu, Nitrite reduction on bismuth modified Pt (111) surfaces in different electrolytic media, *Electrocatalysis* 2 (2011) 255–262, <https://doi.org/10.1007/s12678-011-0053-2>.
- [58] E. Pérez-Gallent, M.C. Figueiredo, I. Katsounaros, M.T.M. Koper, Electrocatalytic reduction of nitrate on copper single crystals in acidic and alkaline solutions, *Electrochim. Acta* 227 (2017) 77–84, <https://doi.org/10.1016/j.electacta.2016.12.147>.
- [59] Y. Wang, H. Li, W. Zhou, X. Zhang, B. Zhang, Y. Yu, Structurally disordered RuO₂ nanosheets with rich oxygen vacancies for enhanced nitrate electroreduction to ammonia, *Angew. Chem. Int. Ed.* 61 (2022), e202202604, <https://doi.org/10.1002/anie.202202604>.
- [60] N. Zhang, J. Shang, X. Deng, L. Cai, R. Long, Y. Xiong, Y. Chai, Governing interlayer strain in bismuth nanocrystals for efficient ammonia electrosynthesis

- from nitrate reduction, ACS Nano 16 (2022) 4795–4804, <https://doi.org/10.1021/acsnano.2c00101>.
- [61] D.J. Campbell, J. Collini, J. Sławińska, C. Autieri, L. Wang, K. Wang, B. Wilfong, Y. S. Eo, P. Neves, D. Graf, E.E. Rodriguez, N.P. Butch, M. Buongiorno Nardelli, J. Paglione, Topologically driven linear magnetoresistance in helimagnetic FeP, npj Quantum Mater. 6 (2021), <https://doi.org/10.1038/s41535-021-00337-2>.
- [62] G. Wen, J. Liang, Q. Liu, T. Li, X. An, F. Zhang, A.A. Alshehri, K.A. Alzahrani, Y. Luo, Q. Kong, X. Sun, Ambient ammonia production via electrocatalytic nitrite reduction catalyzed by a CoP nanoarray, Nano Res. 15 (2021) 972–977, <https://doi.org/10.1007/s12274-021-3583-9>.